Nanoscale

Accepted Manuscript

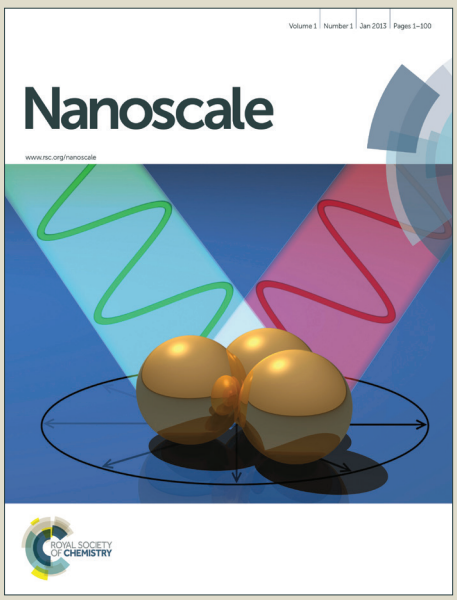

This is an *Accepted Manuscript*, which has been through the Royal Society of Chemistry peer review process and has been accepted for publication.

Accepted Manuscripts are published online shortly after acceptance, before technical editing, formatting and proof reading. Using this free service, authors can make their results available to the community, in citable form, before we publish the edited article. We will replace this *Accepted Manuscript* with the edited and formatted *Advance Article* as soon as it is available.

You can find more information about *Accepted Manuscripts* in the Information for Authors.

Please note that technical editing may introduce minor changes to the text and/or graphics, which may alter content. The journal's standard Terms & Conditions and the Ethical guidelines still apply. In no event shall the Royal Society of Chemistry be held responsible for any errors or omissions in this *Accepted Manuscript* or any consequences arising from the use of any information it contains.

ROYAL SOCIETY OF CHEMISTRY

www.rsc.org/nanoscale

Graphene nanoribbons blends with P3HT for organic electronics

Mirella El Gemayel,[a] Akimitsu Narita,[b] Lukas F. Dössel,[b] Ravi S. Sundaram,[c] Adam Kiersnowski,[b,d] Wojciech Pisula,[b] Michael Ryan Hansen,[b,e] Andrea C. Ferrari,[c] Emanuele Orgiu,[a] Xinliang Feng [b,] Klaus Müllen,[b,*], Paolo Samorì[a,*]*

[a] Nanochemistry Laboratory, ISIS & icFRC, Université de Strasbourg & CNRS, 8 allée Gaspard Monge, 67000 Strasbourg, France

[b] Max-Planck Institute for Polymer Research, Ackermannweg 10, 55124 Mainz, Germany.

[c] Cambridge Graphene Center, Department of Engineering, Cambridge University, 9 JJ Thomson Avenue, Cambridge CB3 OFA, UK

[d] Polymer Engineering and Technology Division Wroclaw University of Technology Wybrzeze Wyspianskiego 27, 50-370 Wroclaw, Poland.

[e] Interdisciplinary Nanoscience Center (iNANO) and Department of Chemistry, Aarhus University, Gustav Wieds Vej 14, DK-8000 Aarhus C, Denmark.

E-mail: samori@unistra.fr, muellen@mpip-mainz.mpg.de, feng@mpip-mainz.mpg.de

Nanoscale Accepted Manuscript

Abstract

In organic field-effect transistors (OFETs) the electrical characteristics of polymeric semiconducting materials suffer from the presence of structural/morphological defects and grain boundaries as well as amorphous domains within the film, hindering an efficient transport of charges. To improve the percolation of charges we blend a regioregular poly(3-hexylthiophene) (P3HT) with newly designed $N = 18$ armchair graphene nanoribbons (GNRs). The latter, that are prepared by a bottom-up solution synthesis, are expected to form solid aggregates which cannot be easily interfaced with metallic electrodes, limiting charge injection at metal–semiconductor interfaces, and are characterized by a finite size thus by grain boundaries, which negatively affect the charge transport within the film. Both P3HT and GNRs are soluble/dispersible in organic solvents, enabling the use of a single step co-deposition process. The resulting OFETs have a three-fold increase in the charge carrier mobilities in blend films, when compared to pure P3HT devices. This behavior can be ascribed to GNRs, and aggregates thereof, facilitating the transport of the charges within the conduction channel by connecting the domains of the semiconductor film. The electronic characteristics of the devices such as I_{on}/I_{off} ratio are not affected by the addition of GNRs at different loads. Studies of the electrical characteristics under illumination for potential use of our blend films as organic phototransistors (OPTs) reveal a tunable photoresponse. Therefore, our strategy offers a new method towards the enhancement of the performance of OFETs, and holds potential for technological applications in (opto)electronics.

Nanoscale Accepted Manuscript

Introduction

Over the past few years, a great effort has been devoted to the development of new organic semiconducting materials, combining solution processability, stability under ambient conditions, and high charge carrier mobility[1-10] for applications in organic electronics and particularly in organic field-effect transistors (OFETs). OFETs can be fabricated by using either small molecules or polymeric semiconductors as electroactive layers. In the latter case, despite the fact that polydisperse molecules can form extended networks for efficient percolation of charges, due to their polycrystalline nature the obtained material is characterized by the presence of structural and morphological defects, grain boundaries and amorphous domains hampering efficient charge transport.[11] To circumvent this problem, polymeric semiconductors have been blended with either small molecules or other (semi)conducting systems.[11-19] By blending different components new functions can be conferred to the material and to the device,[20] benefiting the properties brought about by each component and exceeding its individual performance. Such an effect varies with the degree of phase segregation between the different components in the blend. Among polymeric semiconductors, regioregular poly(3-hexylthiophene) - P3HT is a prototypical system for solution processed OFETs. [21-25] Recently the performance of P3HT based OFETs has been improved by co-deposition with graphene, revealing an increase in charge carrier mobilities over 20 times when compared to the pure P3HT.[26] This enhanced electrical characteristic can be ascribed to the beneficial role of graphene, which builds preferential paths for charge transport, therefore increasing the overall hole mobility,[27] similarly to previous findings in OFETs based on carbon nanotubes with P3HT;[28, 29] however, this was accompanied by a decrease of the on-off current ratio (I_{on}/I_{off}).

Due to the fact that graphene is a zero-gap semiconductor,[30] with high charge carrier mobilities[31], it cannot be used as electroactive component to be incorporated in the channel of a regular OFET. A great deal of efforts have been dedicated to the opening of a band gap in graphene[32]. This was in one way achieved by geometrically confining the 2D graphene via designing graphene nanoribbons (GNRs).[33] Fabrication of GNRs has been predominantly carried out by top-down methods such as lithographic patterning of graphene sheets,[34-36] longitudinal unzipping of carbon nanotubes,[37-39] and chemical extraction from exfoliated graphite.[40] However, these methods lead to the production of GNRs exhibiting a broad (10-100 nm) width distribution[37-39] as well as defective edge structures, resulting in GNRs with non-uniform electronic properties,

Nanoscale Accepted Manuscript

e.g. band gap and ionization potential. In addition, top-down methods for the production of GNRs typically suffer from very low yield, hindering practical applications of the GNRs.[37] In contrast, a bottom-up synthetic approach based on solution-mediated[41-44] and surface-assisted[45] cyclodehydrogenation[46, 47] of tailor-made polyphenylene precursors has been developed, enabling the fabrication of a variety of uniform and structurally defined GNRs with lateral width of ca. 1–2 nm, which possess large and defined band gaps (1.1–1.7 eV).[42, 45] On the other hand, by solution-mediated method it is possible to produce GNRs in a large scale with relatively high yield, as well as to render the GNRs dispersible in organic solvents by installing solubilizing groups at the peripheral positions.[41, 42, 44] It has been theoretically revealed that the absolute value of the valence band, which is related to the ionization potential, decreases as the lateral extension of the GNRs.[48] We have recently reported laterally extended GNR with width of 1.54–1.98 nm, but the absolute value of the valence band of this GNR was estimated to be still higher than that of P3HT, hindering the use of this GNR for the blending with P3HT.[42, 48] Further, the edge of this GNR contains cove-type structure, and the fabrication of broad (~2 nm) and fully armchair edged GNRs has remained a challenge.

In this work we present the solution synthesis of an unprecedented $N = 18$ armchair GNR **1** (Fig. 1a), which possesses a lateral width of ~2.1 nm based on molecular modeling, surpassing all the GNRs hitherto fabricated by the bottom-up synthesis. Remarkably, GNR **1** features an ionization energy (IE) close to that of P3HT, making it the ideal candidate for the present study, in particular to avoid traps and energy barriers within the bi-component film. The edge decoration with long alkyl chains renders GNR **1** dispersible in common organic solvents such as tetrahydrofuran (THF), chlorobenzene and *ortho*-dichlorobenzene (ODCB), enabling its easy integration into organic electronic devices.

GNR **1** has been blended with regioregular poly(3-hexylthiophene) - P3HT (Fig. 1b). It is noteworthy that the alkyl chains exposed at the peripheral positions of GNR **1** provide a good affinity for P3HT, as an attempt to minimize the occurrence of macroscopic phase segregation. This is particularly important because of the problems associated with the propensity of GNRs to form microscopic crystals that cannot be easily interfaced with metallic electrodes, therefore limiting charge injection at metal-(semi)conductor interface. Moreover, these microcrystals are alternated by domain boundaries hampering the charge transport within the film. The effect of the GNRs at different concentrations (in the blend) on the device performance in dark such as the

Nanoscale Accepted Manuscript

field-effect mobility and the I_{on}/I_{off} has been investigated. The influence of illumination with monochromatic light on the electrical characteristics of the device has been studied aiming at exploring the potential use of this blend as active layer in hybrid organic phototransistors (OPTs).

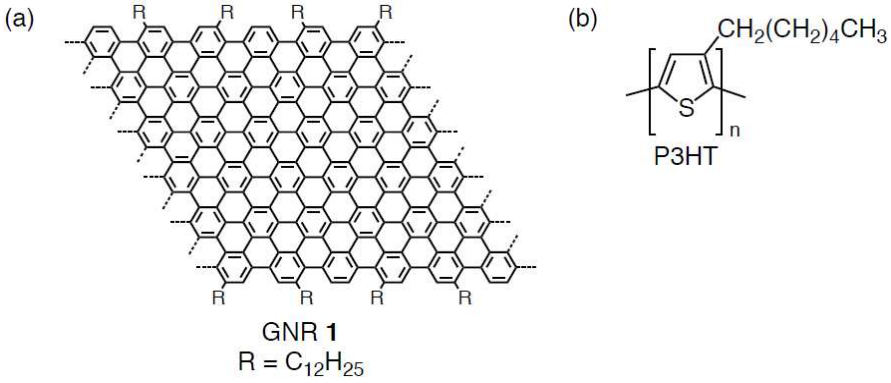

Figure 1: Chemical formulae of (a) GNR **1** and (b) poly(3-hexylthiophene) (P3HT).

Results and discussion

Synthesis of GNR 1

Scheme 1. Synthetic route to GNR 1.[a]

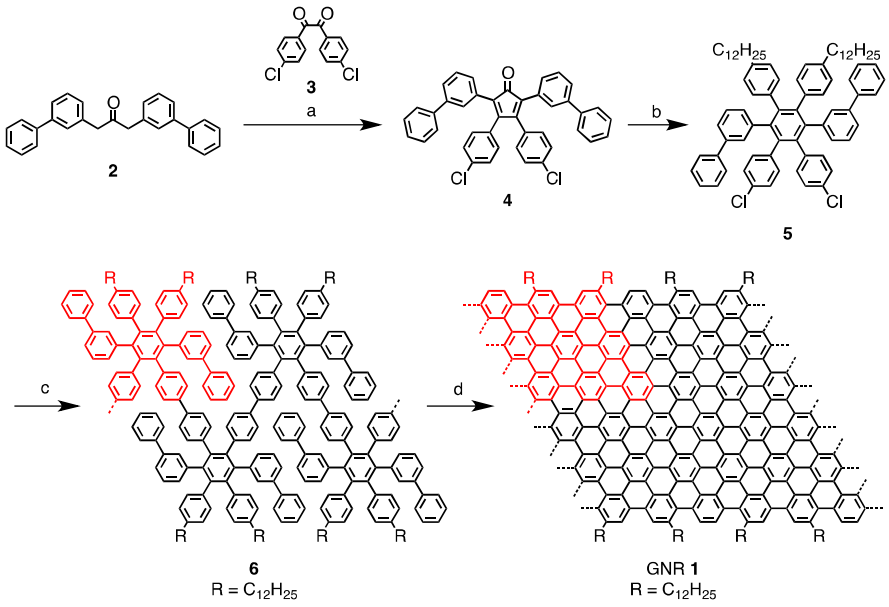

Nanoscale Accepted Manuscript

[a] Reagents and conditions: (a) tetrabutylammonium hydroxide, *t*BuOH, 80 °C, 77%; (b) bis(4-dodecylphenyl)acetylene, Ph_2O, 230 °C, μW, 300 W, 56%; (c) bis(cycloocta-(1,5)-diene)nickel(0), cycloocta-(1,5)-diene, 2,2'-bipyridine, toluene/DMF, 80 °C, 86% (before fractionation); (d) $FeCl_3$, CH_2Cl_2/CH_3NO_2, rt, 98%.

Scheme 1 portrays the synthetic route towards GNR **1**. Our recent study has shown that the *AA*-type Yamamoto polymerization from one single monomer[42, 49, 50] is more efficient for the synthesis of high-molecular-weight polyphenylene precursors than the A_2B_2-type Suzuki polymerization that requires heterogeneous reaction condition involving two different monomers.[41, 44, 51] Very recently, *AB*-type Diels–Alder polymerization has proved to be superior to transition-metal-catalyzed couplings for synthesizing long (>100 nm) GNRs, but the width of GNR is only about 1 nm.[52] In order to build up laterally extended, N = 18 armchair GNR **1** by employing Yamamoto polymerization, dihalogenated monomer **5** was designed (Scheme 1). Unlike previously reported monomers that lead to GNRs with the same widths as the monomers,[42-44, 52] the polymerization of monomer **5** with an *o*-terphenyl-based backbone structure would yield laterally expanded polyphenylene precursor **6** with twice the width of the monomer. Precursor **6** would be "graphitized" and "planarized" into GNR **1** with high structural definition albeit slight structural isomerization at the ends of the GNRs (Scheme S2). For the synthesis of monomer **5**, cyclopentadienone **4** was first prepared by Knoevenagel condensation of di(3-biphenylyl)acetone (**2**) and 4,4'-dichlorobenzil (**3**), and then subjected to Diels-Alder reaction with bis(4-dodecylphenyl)acetylene to yield monomer **5** (Scheme 1). Subsequently, Yamamoto polycondensation of monomer **5** was performed employing a standard protocol,[42, 49, 50] followed by fractionation using recycling preparative size exclusion chromatography (SEC) to provide precursor **6**. Weight-average molecular weight (M_w) and polydispersity index (PDI) of precursor **6** were estimated by a SEC analysis to be ca. 10000 $gmol^{-1}$ and 1.4, respectively, against polystyrene (PS) standards (Fig. 2a). When the poly(*p*-phenylene) (PPP) standard calibration was applied, M_w of ca. 7300 $gmol^{-1}$ and PDI of 1.3 was obtained. Considering the kinked and flexible polyphenylene backbone structure of precursor **6** with long alkyl chains at the peripheral positions, the actual M_w of **6** presumably lies between these two values, i.e. 7300–10000 $gmol^{-1}$. Matrix-assisted laser desorption/ionization time-of-flight (MALDI-TOF) mass spectrometry (MS) analysis of precursor **6** showed a regular mass pattern extending up to ~20000 $gmol^{-1}$, which corresponds to the molecular weight of ~20 repeating units (Fig. 2b). Based on this result, the longitudinal length of the resulting GNR **1** could be estimated to be up

Nanoscale Accepted Manuscript

to ca. 10 nm. It should be noted however that this is most probably not the highest value, taking into account the limitation of MALDI-TOF MS for the analysis of large polymers with broad molecular weight distribution.[41, 42, 53]

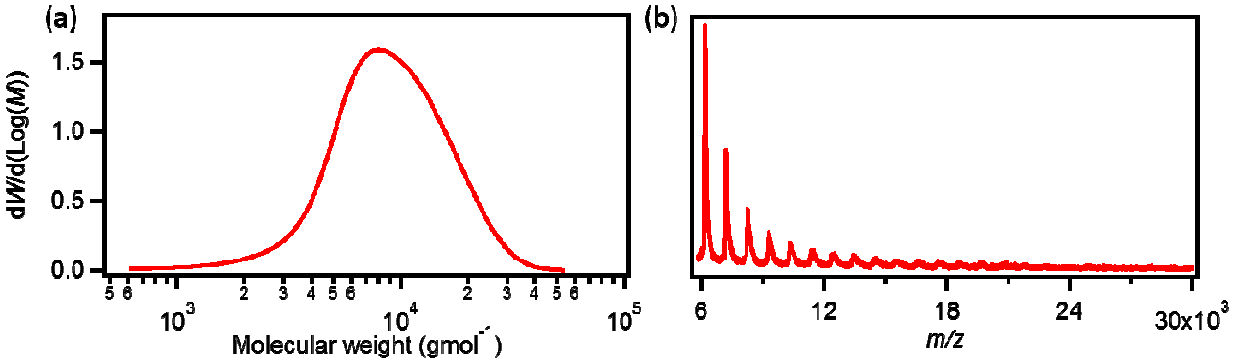

Figure 2: (a) Molecular weight distribution of polyphenylene precursor **6** (SEC analysis, eluent: THF, polystyrene standard). (b) Linear-mode MALDI-TOF MS spectrum of polyphenylene precursor **6**.

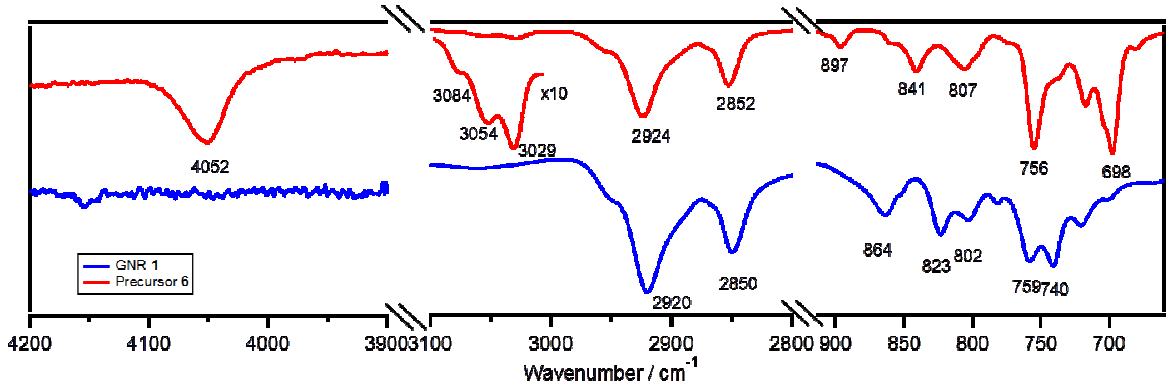

Figure 3: Representative FTIR spectral regions of polyphenylene precursor **6** (red) and GNR **1** (blue).

The intramolecular cyclodehydrogenation of precursor **6** was carried out by an established method, applying iron (III) chloride as the Lewis acid and oxidant in a mixture of dichloromethane and nitromethane.[41-44, 47] MALDI-TOF MS analysis of GNR **1** in linear mode displayed a regular mass pattern similar to that of precursor **6** (Fig. S4 in the ESI). Although the peaks were strongly broadened, the interval was roughly ~1000 $gmol^{-1}$, corresponding to the molecular weight of one repeating unit of GNR **1**, i.e. 991 $gmol^{-1}$. More accurate analysis as well

Nanoscale Accepted Manuscript

as detection of mass exceeding 15000 $gmol^{-1}$ was not possible most probably due to the strong self-association tendency of larger GNRs and fragmentations at higher laser powers.[42, 53]

Comparison of *Fourier* transform infrared (FTIR) spectra of precursor **6** and GNR **1** displayed disappearance of the band from the rotation of free phenyl rings at 4052 cm^{-1}, as well as strong attenuation of the signal triad from aromatic C-H stretching vibrations at 3029, 3054, and 3084 cm^{-1}, after the cyclodehydrogenation (Fig. 3).[41, 42, 54] Further, out-of-plane (*opla*) C-H deformation bands in the fingerprint region such as at 698, 841, and 897 cm^{-1} vanished, validating the disappearance of mono- and di-substituted benzene rings.[54, 55] These results indicated the high efficiency of the cyclodehydrogenation of precursor **6** leading to successful formation of GNR **1**.

To further characterize the cyclodehydrogenation of precursor **6** into GNR **1**, we have used liquid- and solid-state ^{1}H NMR spectroscopy as summarized in Figure 4. This analysis makes it possible to follow the structural changes before and after cyclodehydrogenation, since the ^{1}H chemical shift (position and line width) is known to be a highly sensitive probe for non-covalent interactions.[56-59] The ^{1}H NMR spectra in Figure 4a and b unambiguously reveal that the precursor **6** possesses a semi-flexible/semi-rigid structure due to the fact that the overall ^{1}H line width from the polyphenylene groups at ~7.0 ppm is almost unchanged, when going from the liquid- to the solid-state NMR spectrum (Figure 4a and b, respectively). After the cyclodehydrogenation, the ^{1}H magic-angle spinning (MAS) NMR spectrum of GNR **1** shown in Figure 4c includes significantly broadened ^{1}H resonances, where, in particular, those related to the aromatic signals are shifted to higher frequency (or equivalently to lower field). The broad nature and shift of the aromatic ^{1}H signals demonstrate that these are part of an extended π-conjugated system, [60, 61] and that GNR **1** behaves like a rigid solid in agreement with the formation of GNRs. Figure 4d and e display the 2D ^{1}H-^{1}H double quantum-single quantum (DQ-SQ) NMR correlation experiments mapping out the spatial connectivities between the different ^{1}H signals for precursor **6** and GNR **1**.[62, 63] For precursor **6**, the 2D ^{1}H-^{1}H DQ-SQ spectrum includes narrow ^{1}H-^{1}H correlation signals between polyphenylene groups as well as between the polyphenylene groups and the dodecyl side chains as one might expect for a flexible structure. However, after the cyclodehydrogenation, GNR **1** shows a broad, stretched split ridge of ^{1}H-^{1}H correlation signals close to the spectrum diagonal in the range between ~9-12 ppm (Fig. 4e), in addition to a clear, albeit broad ^{1}H-^{1}H correlation between aromatic protons at ~6-9 ppm and

Nanoscale Accepted Manuscript

those of the dodecyl side chains. Based on these spectral differences we can make the assignment shown in Figure 4f, where the high-frequency part is assigned to the protons at the end of GNR **1** (blue) and the lower-frequency part to the protons of the edge (red) in close spatial proximity to the dodecyl side chains. Note that the edge protons (red) of GNR **1** only show a small shift of ~1-2 ppm to high frequency when compared to precursor **6**, while a much larger shift of ~2-5 ppm is observed for the end protons (blue). These differences illustrate that the bulk sample of GNR **1** is heterogeneously packed, shifting the ^{1}H signals as a result of the different magnitudes for the aromatic ring currents of stacked GNRs.[64, 65]

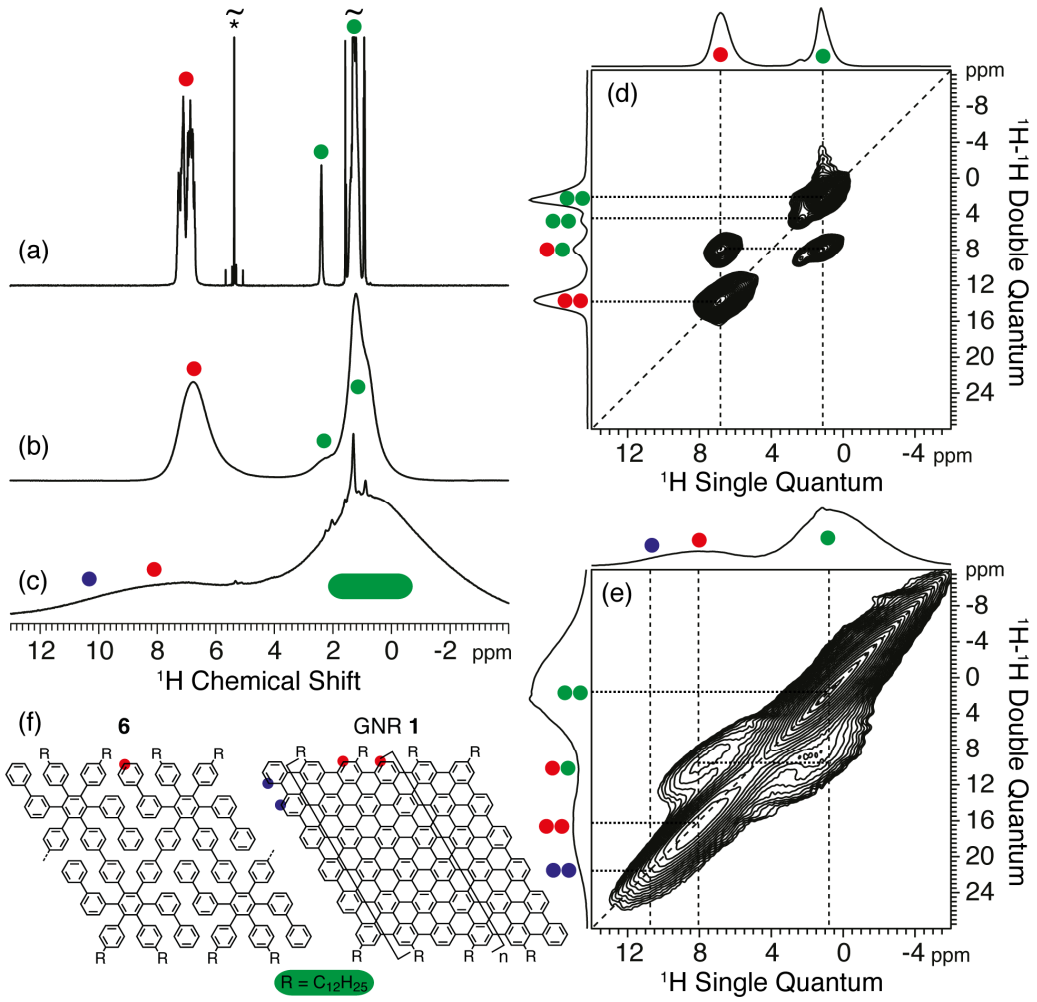

Figure 4. Liquid- and solid-state ^{1}H NMR spectra of (a) precursor **6** in CD_2Cl_2, and (b, c) solid samples of precursor **6** and GNR **1**, respectively. The 2D ^{1}H-^{1}H DQ-SQ correlation spectra of (d) precursor **6** and (e) GNR **1** were recorded using two rotor periods of DQ recoupling. The ^{1}H signals are assigned using the color code given in (f); all the aromatic signals of **6** are represented by the red color. The liquid-state spectrum in (a) was recorded at 7.05 T (300.13 MHz for ^{1}H), while the solid-state NMR experiments in (b-e) were obtained at 16.45 T (700.21 MHz for ^{1}H)

Nanoscale Accepted Manuscript

using a MAS frequency of 59524 Hz. The asterisks in (a) mark the residual proton signals of CD_2Cl_2. The sharp signals in (c) represent residual solvent present in the sample.

The successful conversion of the precursor **6** into GNR **1** was further verified by investigation of a model monomer **S4**, for which the efficient cyclodehydrogenation was demonstrated by the combination of ^{1}H NMR and MALDI-TOF MS analysis (See Supporting Information, SI).

GNR **1** could be easily dispersed in common organic solvents such as THF, chlorobenzene, and ODCB by applying mild sonication to give brown dispersions. Such dispersions of GNR **1** with typical concentration up to ~1 mg/mL in ODCB were stable approximately for one week without apparent precipitation. The UV–vis absorption spectrum of a dispersion of GNR **1** in ODCB showed an absorption maximum at 410 nm with the absorption edge at ~800 nm, corresponding to the optical bandgap of ~1.6 eV (Figure S5). Subsequently, different volumes of such dispersion in ODCB were mixed with solutions of P3HT for the fabrication of GNR-P3HT blend films with various GNRs loading ratio by co-deposition.

Electrical, structural and morphological characteristics in dark

First we will discuss the electronic and electrical characterization of the devices in dark followed by a discussion about the structure of the films.

Nanoscale Accepted Manuscript

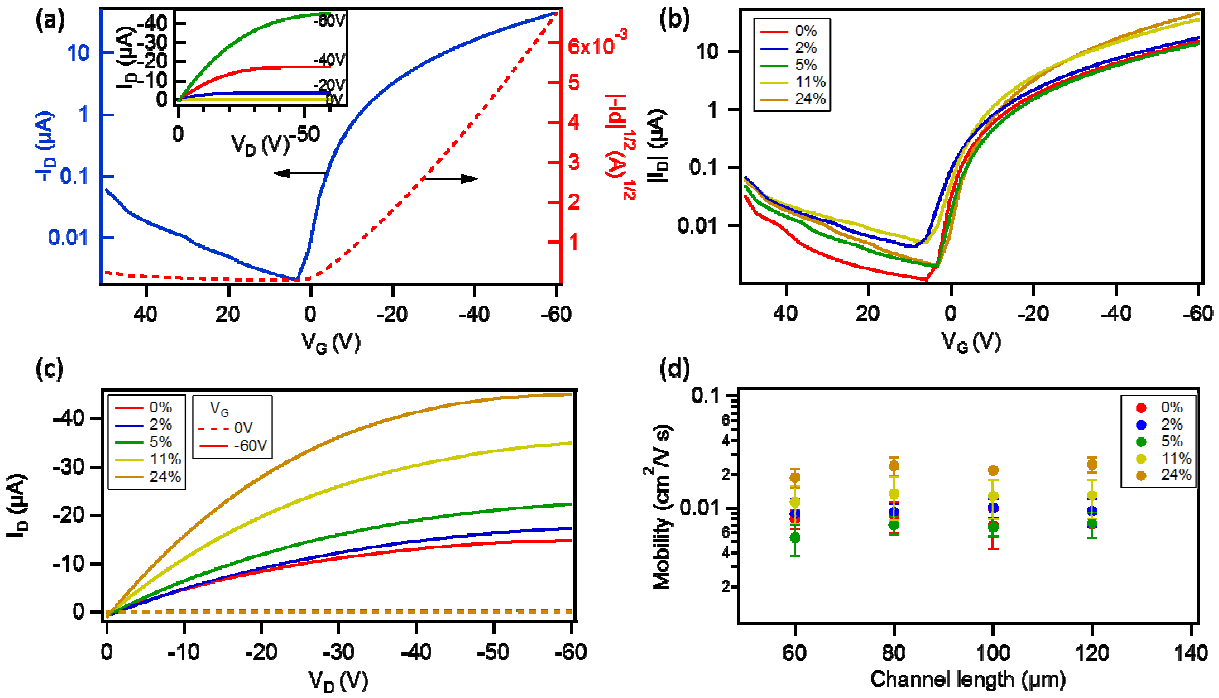

Figure 5: (a) Transfer characteristics of bottom-gate bottom-contact device (***L***=120 µm) prepared by blending 24% of GNRs with P3HT (left axis in the log scale) and the inset shows its output characteristics. (b) Transfer characteristics of bottom-gate bottom-contact devices (***L***=120 µm) prepared by different blend percentages of GNRs with P3HT, and (c) their output characteristics (solid line at V_G=–60 V and dashed line at V_G=0 V; the rest of data at V_G =–20 V and –40V have been omitted for clarity). (d) Variation of the field effect mobility (left axis in the log scale) with the channel length (60, 80, 100 and 120 µm) at different blend percentages of GNRs with respect to P3HT.

Ambient Photoelectron spectroscopy (PS) measurements of the pristine GNR **1** drop casted film provided a HOMO level of 5.010±0.063 eV being close to that of P3HT, i.e. 4.860±0.015 eV. Thereby, this result makes GNR **1** an ideal candidate for our case study.

Then we fabricated devices at various GNRs loading ratio (0, 2, 5, 11 and 24 wt% with respect to P3HT), having different channel length (***L***) ranging from 60 µm to 120 µm. Figure 5a displays transfer characteristics of a 120 µm channel length device with 24% GNRs with its output characteristics shown as inset, the device exhibits a typical p-type behavior. The extracted hole mobility (from the saturation regime at V_D=–60 V), threshold voltage (V_{th}) and I_{on}/I_{off} amounted to 2.8×10^{-2} $cm^2 \cdot V^{-1} \cdot s^{-1}$, –8.9 V and ~$10^3$ respectively. The same channel length device based on pristine P3HT was also studied (transfer and output characteristics are shown in Fig. S6 in the ESI). Interestingly, the only parameter that exhibited a notable change is the field-effect mobility

Nanoscale Accepted Manuscript

$\boldsymbol{\mu}$, which amounted to 7.3×10^{-3} $cm^2 \cdot V^{-1} \cdot s^{-1}$. This result shows that the performance of the device is enhanced in the presence of GNRs. Such an improvement can be ascribed to i) the percolation pathway for the charges provided by the GNRs, or ii) the ionization energy of the 24% blend as determined by ambient PS which surprisingly amounts to 4.790±0.016 eV (i.e. it was lowered by 0.07 eV as compared to the pure P3HT 4.860±0.015 eV), thus it is better matching the workfunction of the Au electrodes (4.810±0.020 eV) enabling a better charge injection. A comparison of the transfer characteristics (at V_D=–60 V) of the devices with the same $\boldsymbol{L}$=120 µm at different concentrations of GNRs is shown in Fig. 5b. It reveals an increase in the I_d with increasing the relative amount of GNRs up to a factor of 3 when comparing the 24% blend with the pristine devices (0% blend). Such a trend is also evident in Fig. 5c which compares the output characteristics of the same blend device at V_G= 0 V (dashed line) and at V_G=–60 V (solid line).

Figure 5d (see also Fig. S7 in the ESI) shows the high variation of hole field-effect mobility at different concentrations of GNRs and for devices with different $\boldsymbol{L}$. In particular, at 2 and 5% loadings, the field-effect mobility is comparable to that of the devices with pristine P3HT. Interestingly, the mobility increased approximately by a factor of 1.7 when the content of GNRs augments to 11%, and by a factor of 3 at 24% with respect to P3HT. The enhanced performance can be attributed to the above mentioned reasons and mainly to the amount of GNRs that can facilitate the charge transport within the conduction channel as observed in similar studies on P3HT blend with graphene[26] or with functionalized carbon nanotubes.[29] Enhanced performances were also observed for other p-type polymers printed on the top of a graphene layer inside the channel.[66] In fact, it has been demonstrated that when blending P3HT with another semiconductor, there is a critical concentration for the enhancement of the mobility.[28, 67] When comparing all the devices at different blend % and different $\boldsymbol{L}$ spanning from 60 µm to 120 µm, the average V_{th} was found to range between 2 and –5 V, and to be slightly higher (up to –8 V) for those with 24% of GNR **1**. Significantly, the average I_{on}/I_{off} ranged between 10^3 and 10^4, and appeared being uneffected by the presence of GNRs (see Fig. S8 in the ESI), unlike blends with graphene where the I_{on}/I_{off} markedly decreases at higher concentrations.[26] Electrical characterization was also performed on shorter channel lengths ranging from 2.5 µm to 20 µm, the results being reported in Fig. S9 in the ESI.

Nanoscale Accepted Manuscript

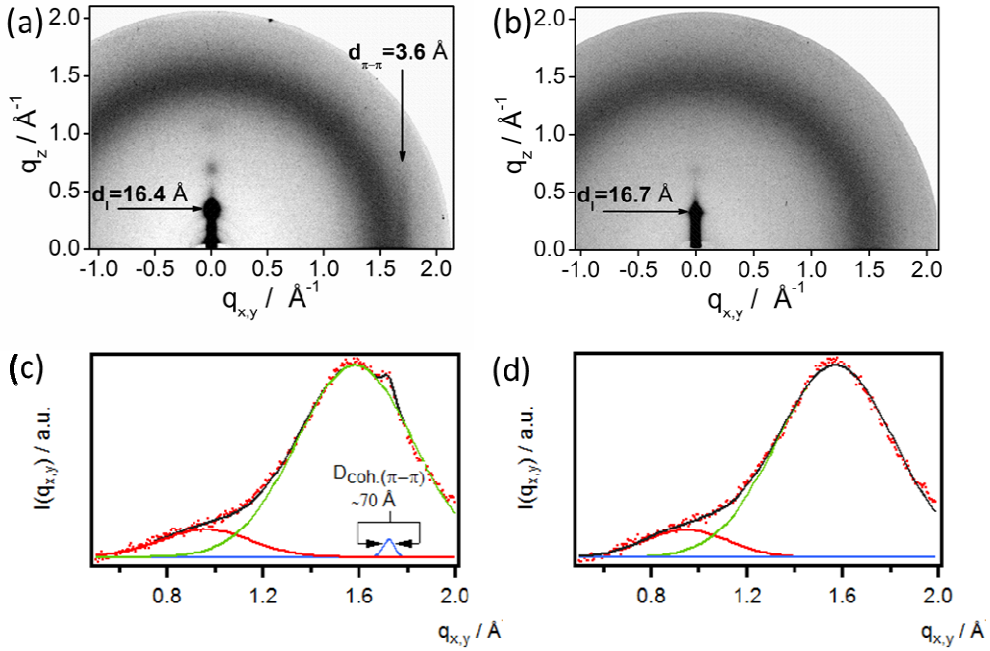

Figure 6: GIXD patterns of the P3HT film (a), P3HT+2 wt.% GNR (b) and the corresponding horizontal integrations of P3HT (c) and the blend (d).

To gain further insight into the relationship between electrical properties and structure within the blend films, Grazing Incidence X-ray Diffraction (GIXD) measurements were carried out on the spin-coated films. This reveals that the addition of GNR **1** strongly influences the order within P3HT films. In the pattern recorded for the monocomponent P3HT film (Fig. 6a) the *h*00 series, corresponding to the interchain distance measured in the plane of aromatic rings is discernible up to the third diffraction order. Another characteristic peak, originating from the π-π stacking of P3HT is visible on the equator, indicating that in the pure P3HT film the macromolecules adopt an edge-on orientation in the crystalline domains. The chain-to-chain distance (16.4 Å), the π-stacking distance (3.6 Å) as well as the approximated coherence length of the π-π stacking derived from GIXD data (~70 Å; Fig. 6a,c) are typical for P3HT films.[68-70] The addition of GNR to P3HT affects the arrangement of the crystalline structure of the polymer. The absence of characteristic equatorial reflections at $q_{x,y}\approx1.72$ Å^{-1} related to the π-stacking reflection in XRD patterns of all the blends (Fig. 6b,d) indicates that even the presence of small amount of GNR such as 2 wt.-% hinders the formation of coherent π-stacks. Increasing amounts of the GNR

Nanoscale Accepted Manuscript

cause also a gradual decrease in the integral intensity of the *100* reflection (at q_z=0.377 $Å^{-1}$), providing an evidence for a decrease in lamellar ordering of P3HT macromolecules and hence in the overall crystallinity of the polymer. Unfortunately, a strong diffuse scattering of X-rays on the GNR overlaps with P3HT peaks, which disables a quantitative analysis of the polymer crystallinity. On the other hand, such a strong scattering suggests the existence of a large interface area between the GNR and P3HT. Increasing the GNR content beyond 5 wt.% causes almost complete disappearance of diffraction features from the crystalline fraction of P3HT, which indicates that at the higher content of GNR no significant polymer crystals are formed. By and large, it is suggested that the increase of the mobility in the blend can be attributed to the presence of GNRs and aggregates thereof, providing favorable pathways for the transport of charges counteracting the effect of the decrease crystallinity in the P3HT domains upon addition of GNR.

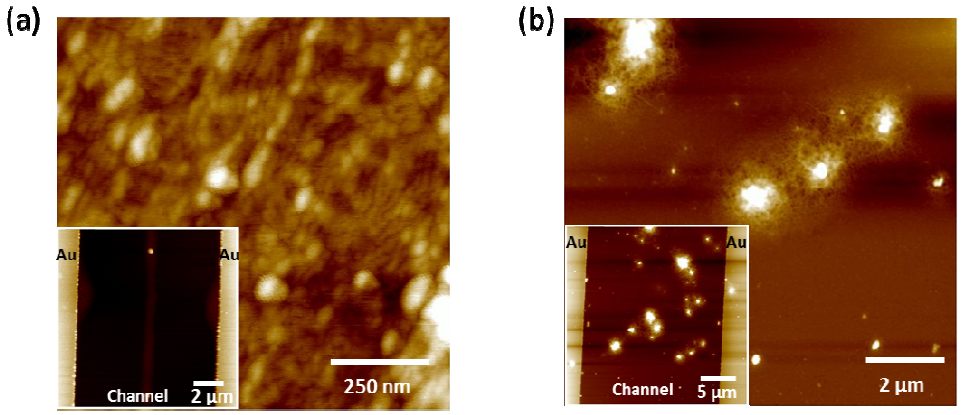

Figure 7: AFM images scanned inside the channel of films of: (a) pristine P3HT and (b) 24% GNR with P3HT. The insets show the scan at a larger scale. Z-scales: (a) 17 nm, (b) 75 nm, inset (a) 47 nm, inset (b) 92 nm.

As the q-range in the GIXD experiments allowed studying structures with length scales up to a very few nanometers, in order to analyze the occurrence of possible phase separation on a length scale ranging from a few nanometers up to a few tens of micrometers we used atomic force microscopy in the tapping mode (TM-AFM). The pristine P3HT film from ODCB solution is homogeneous featuring a fibrillar and grain-like structures on the tens of nanometers scale (Fig. 7a). At 24%, the P3HT/GNRs films are inhomogeneous due to the aggregation of the GNRs as shown in Fig. 7b. These aggregates having a height ranging from 60 to 200 nm and a width spanning from 0.6 to 2 µm, were found to be randomly distributed within the polymer matrix. Their frequency of occurrence inside the channel, i.e. the number of aggregates located in the

Nanoscale Accepted Manuscript

source-drain gap, was proportional to the concentration of GNRs; conversely, the aggregate size was found being independent on the concentration (see Fig. S11 in the ESI). This finding clarifies how the aggregates of GNRs, and not single GNRs, act as "electronic bridge" between P3HT domains. Because of the notably high propensity of our GNRs to undergo aggregation when deposited on a solid surface, single component polycrystalline structures are obtained which are difficult to be characterized; this result is in line with observations on similar liquid phase-processable GNRs.[52] It is indeed surprising the mild increase in field-effect mobility we have measured upon blending P3HT with the GNRs, given that it is known that a 2 nm wide GNR can exhibit a mobility around 100 $cm^2 \cdot V^{-1} \cdot s^{-1}$.[71] Yet, a maximum field-effect mobility 3.25 x 10^{-2} $cm^2 \cdot V^{-1} \cdot s^{-1}$ was observed for a similar arm-chair GNR deposited from ODCB.[72] Consequently, the reason for the limited increase in mobility is likely the simultaneous effect of decreased crystallinity with the P3HT film upon blending and the charge scattering when encountering GNR aggregates.

Electrical characteristics under illumination

Nanoscale Accepted Manuscript

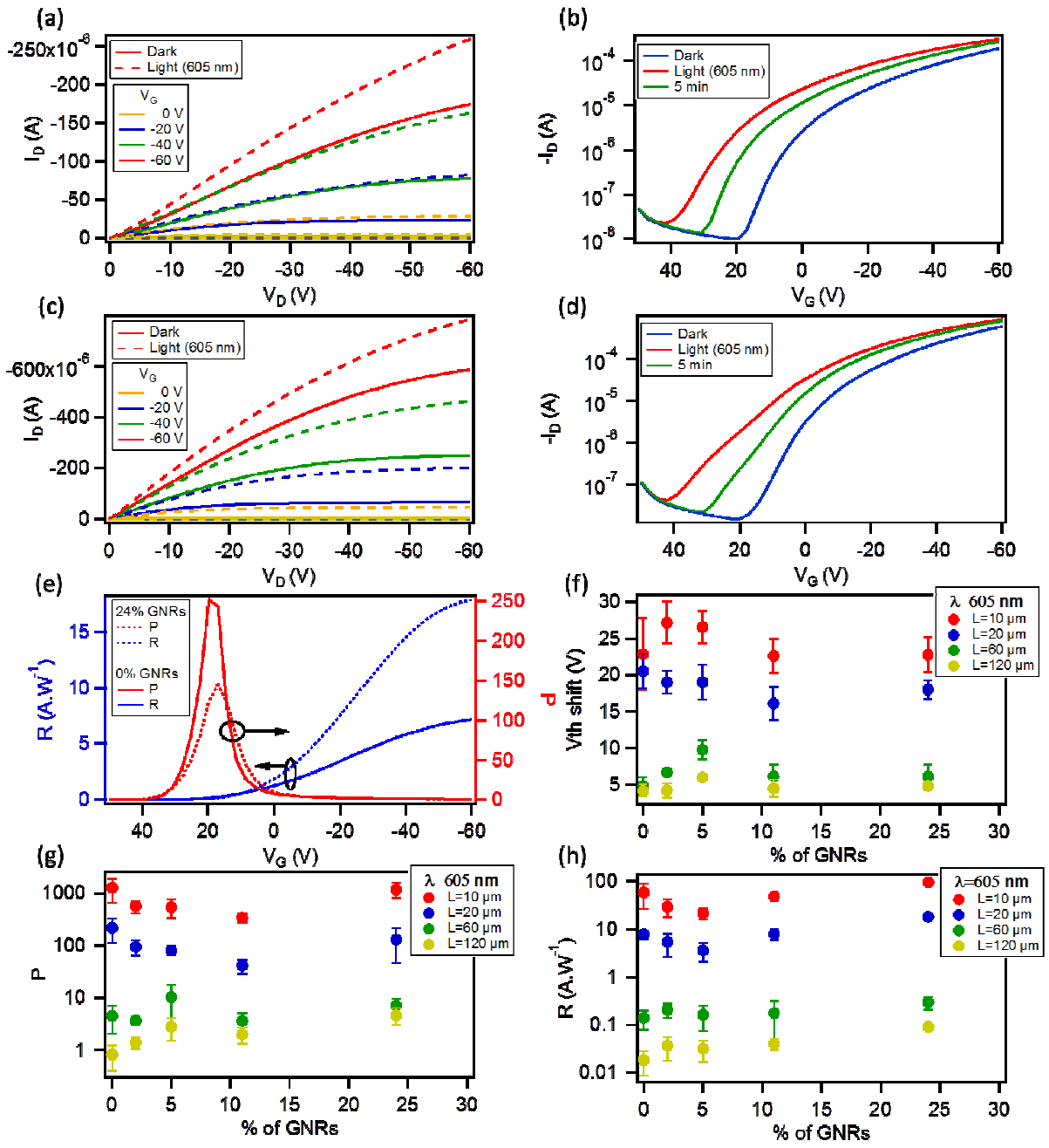

Figure 8: Comparison of (a) output and (b) transfer characteristics at V_D = –60 V of Pristine P3HT OFET**;** (**c**) output and (**d**) transfer characteristics at V_D = –60 V of a device with 24% GNR blend with P3HT with the same channel length ***L***=20 µm measured in dark and under monochromatic light (λ=605 nm; 8.17 mW/cm^2). (e) Variation of the responsivity ***R*** (blue curves) and photosensitivity ***P*** (red curves) with V_G at V_D = –60 V at λ=605 nm for OFETs (***L***= 20 µm) with 0% (solid lines) and 24 % blends of GNRs (dashed lines). (f) Threshold voltage shift under illumination with monochromatic light (λ=605 nm; 8.17 mW/cm^2) for 4 channel lengths (***L***=10, 20, 60 and 120 µm) OFETs based on different blend percentages of GNRs with respect to P3HT. (g) Photosensivity (extracted at V_G=20 V), and (h) responsivity of these devices (extracted at V_G=-60 V) both at V_D = –60 V. Left axis is expressed in log-scale.

Nanoscale Accepted Manuscript

Measurements of the photoresponse under illumination at 605 nm and 560 nm were carried out to investigate both the potential application of these OFETs in optoelectronics and the influence of the GNRs on the photo-generated carriers. The two wavelengths were chosen because they correspond to two absorption peaks of the films (see Fig. S12 in the ESI).

The difference in output (I_D-V_D) and transfer (I_D-V_G) characteristics of a 0% and 24% OFET (***L***=20 µm) in dark and under illumination with monochromatic light (8.17 mW/cm^2) at λ=605 nm is illustrated in Fig. 8a-d. The electrical characteristics of a pristine P3HT based device, i.e. with 0% GNR in the blend, is shown in Fig. 8a,b. It displays an increase of the drain current in the I_D-V_D and I_D-V_G curves upon irradiation with monochromatic light as a result of the photogeneration of excitons that dissociate into free charge carriers which subsequently move towards the electrode under the influence of the electric field.[73] The same was observed for the 24% blend. The only difference is that at V_G=20 V (V_D=–60 V) the ratio of the photocurrent (I_{ph}) (calculated by subtracting the current in dark (I_{dark}) from the current under light (I_{light}, i.e. $I_{ph}=I_{light}-I_{dark}$) to the current in dark (I_{dark}) was 251.71 for the device with 0% GNR (see Fig. 8b also Fig. 8e red plot with solid line) whereas it was much lower (145.1) for the device with 24% blend (see Fig. 8d also Fig. 8e red plot with dashed line). This ratio, called photosensitivity ***P***:

$$P = \frac{I_{light} - I_{dark}}{I_{dark}} \qquad (1)$$

is one of the key figures of merit of an organic phototransistor. Another important parameter is the responsivity ***R***:

$$R = \frac{I_{light} - I_{dark}}{E \cdot A} \qquad (2)$$

where ***E*** is the irradiance of the incident light and ***A*** is the effective device area. In contrast to ***P***, ***R*** value (18 A·W^{-1}) of the device with 24% blend (Fig. 8e blue plot with dashed line) was more than twice higher than that of the 0% blend (7.2 A·W^{-1}) at V_G=–60 V (V_D=–60 V) (Fig. 7e blue plot with solid line). Considering Eq. 2 and since ***E*** and ***A*** are equal for both devices, higher ***R*** in the case of 24% blend indicates that I_{ph} is higher than that of the 0%. This might be due to (i) the presence of more carriers resulting from a better dissociation of excitons in the presence of GNRs, and/or (ii) the GNRs at this concentration help in conducting more charges hence collecting more photogenerated ones at the electrodes. To assess the validity of these

Nanoscale Accepted Manuscript

propositions, OFETs with different channel lengths (***L***=10, 20, 60 and 120 µm) and different loads of GNRs with respect to P3HT (0%, 2%, 5%, 11% and 24%) were studied under this wavelength. We observed the highest photoresponse, as quantified by a ***R***= 94.46 $A \cdot W^{-1}$ and a ***P***=1463.26 for the 24% device for the 10 µm channel length. Such a photoresponse decreases by several orders of magnitude with increasing the channel length (see Fig. 8f, g and h). This is in line with the previous study done on perylenebis(dicarboximide)s (PDIs) based organic phototransistors.[74] When considering the devices with ***L***=10 µm at different blend percentages, under illumination, the average threshold voltage shift was in the same range, ca. 23 V, for 0%, 11%, and 24% blends. However, it was slightly higher, ca. 27 V, for 2% and 5% blends. A similar trend was observed for all the channel lengths except for ***L***=20 µm devices (see Fig. 8f). In fact the origin of the threshold voltage shift has been attributed to (i) a reduction in energy level bending resulting from the Fermi level which moves close to the highest occupied molecular orbital under illumination,[75] (ii) the change in the trap states of the semiconductor[76-79]. Recently it was demonstrated that the apparent shift comes from the increase in the total current because of the photo-generated current[80]. In our case, under illumination, one cannot detect any trend in the V_{th} shift with increasing the percentage of GNRs and with the channel length, probably due to the random distribution of the aggregates of GNRs inside the channel and the difference in their size as shown by AFM images. On the one hand, in OFETs with ***L***=10 and 20 µm, the average photosensitivity ***P*** (Fig. 8g) decreases with the increasing amount of GNRs and this is more significant at 2% and 5% (as compared to 0%) contrarily to the devices with *L*=60 and 120 µm. On the other hand, the responsivity ***R*** for ***L***=10 and 20 µm (Fig. 8h) decreases with increasing the % of GNR in the blend except for 24%, where it is higher than that of the 0% blend by a factor of two, approximately similarly to the devices with ***L***=60 and 120 µm; however, in the latter case ***R*** increases with the blend percentage. This demonstrates that the ability of a device (with short ***L***) to convert light into electric current is three times larger in the presence of GNRs at 24%.

Nanoscale Accepted Manuscript

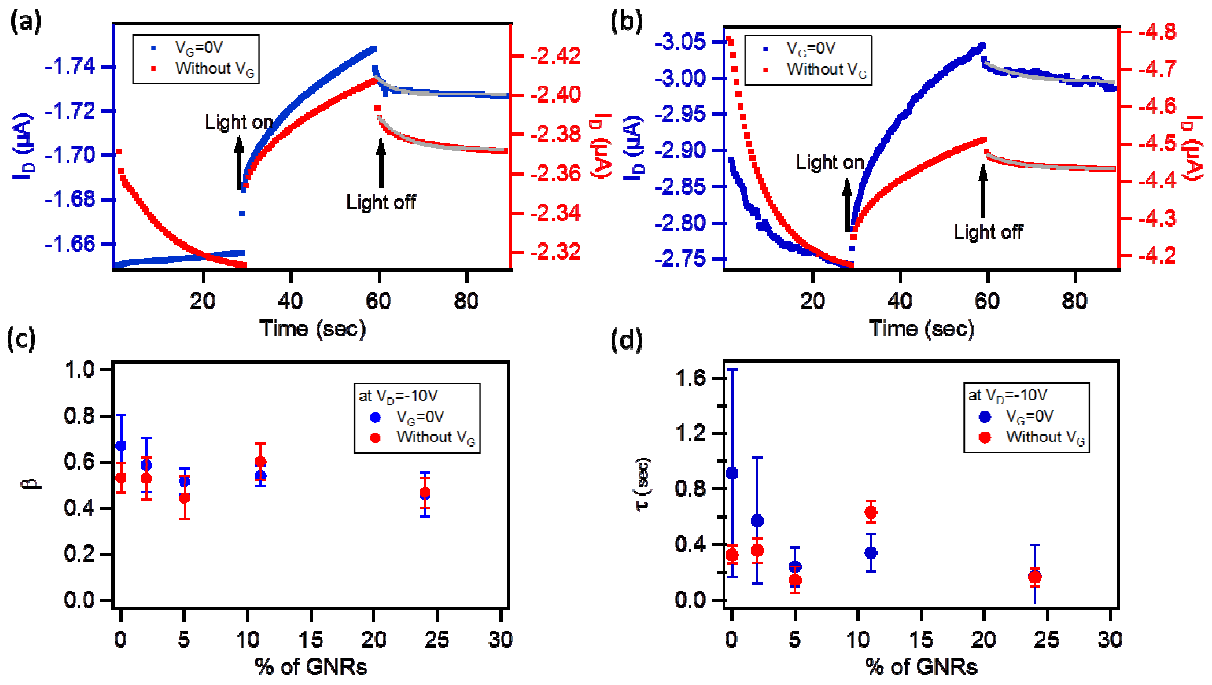

Figure 9: (a) Relaxation characteristics of the photoinduced current after irradiation with a monochromatic light (λ=560 nm, 9.44 mW/cm^2) (light on at 30 sec, light off at 60 sec) for a 0% blend, and (b) 24% blend of Graphene nanoribbons with respect to P3HT). The gray line is the fitting by Kohlrausch's law. Average variation of: (c) the exponent β (indicating the degree of the disorder of the material), and (d) the relaxation lifetime τ at different blend percentages (done on 5 to 6 devices for each blend %).

The photoresponse was also conducted at λ=560 nm (9.44 mW/cm^2), corresponding to the maximum absorption of the P3HT films as shown in E12 in the ESI. This is only seen for devices with 10 and 20 μm channel lengths while a much lower photoresponse is seen for ***L***=60 and 120 μm. By comparing the trend with the GNRs % for the responsivity and photosensivity to that at 605 nm, we find that ***R*** values are similar to those at 605 nm (Fig. S13a in the ESI), whereas ***P*** values were slightly higher (Fig. S13b in the ESI). Only a small increase in the photoresponse is observed by lowering the wavelength of the irradiation, which can only be explained by (i) the greater energy of photons of λ=560 nm when compared to λ=605 nm, and (ii) the small difference in the absorbance peaks at λ=560 nm and 605 nm (Fig. S12 in the ESI). It is also important to note that for pristine P3HT devices, ***R*** and ***P*** values obtained in our case (prepared by spin-coating) with ***L***=10 μm are close to the ones reported in literature.[73, 81] This suggests that the use of a monochromatic light source with a wavelength matching the peak of absorption of the semiconductor is expected to result in a higher photoresponse as compared to the use of a broad band illumination (see Fig. S13d in the SI, where the same device was tested

Nanoscale Accepted Manuscript

under white light and monochromatic light at 605 and 560 nm). The field-effect mobility of the devices studied at both wavelengths remained relatively unaffected under illumination as compared to the one in dark (see Fig. S13c in the ESI).

Furthermore, after 5 min of switching off the light, both devices at 0 and 24% did not regain their initial characteristics due to a photoinduced memory effect (Fig. 8b and 8d green plots). In view of this finding, we extended our study to the examination of this slow relaxation at different blend percentages as a function of the gate voltage (with V_G=0 V and without V_G). Figure 9a,b depict the relaxation mechanism of the photoinduced charges after illumination for 30 sec for a 20 μm device with 0 and 24% blend respectively, measured at V_D=–10 V. In both cases, the photoinduced current decreases slowly once the light source is switched off at t=60 sec (see Fig. 9a and b) and in the same manner regardless the application (blue plots) or not (red plots) of a gate bias. The same result was observed for the other blend percentages. This decay has been reported for regioregular P3HT[82, 83] and fitted to a stretched-exponential behavior (Kohlrausch's Law) (grey curves in Fig. 9a and b) :

$$\sigma(t) = \sigma_0 \cdot \exp\left[-\left(\frac{t}{\tau}\right)^{\beta}\right] \qquad 0 < \beta < 1 \qquad (3)$$

where σ is the conductivity, τ is the relaxation lifetime and the exponent β that indicates the degree of the disorder of the material. Figure 9c portrays the average of the extracted values for β for different blend percentages. It reveals that β values are almost in the same range considering the error of the fitting and the error bars with or without V_G. As for the variation of the relaxation lifetime τ with the concentration of GNRs, the results are displayed in Fig. 9d. The average τ values are found to depend on the fitting parameters, the blend % and the gate bias. If no gate bias is applied, τ does not following any trend with the blend %; whereas at V_G=0 V, when considering the error bars, there is not a clear trend when increasing the blend %. This can be attributed to the random distribution of the GNRs within the P3HT domains inside the channel, which will result in the variation of the trap densities, thus affecting τ. In fact it was shown that the relaxation mechanism depends on the bulk trap densities, the insulator-semiconductor interface, the diffusion rate of the photoinduced charge carriers, the gate voltage[83] and mainly the presence of negatively charged electron accepting impurities[82] present in P3HT. This might

Nanoscale Accepted Manuscript

explain the difference observed with τ and makes it difficult to understand if the aggregates of GNRs help in increasing the recombination rate of holes.

Photocurrent mapping

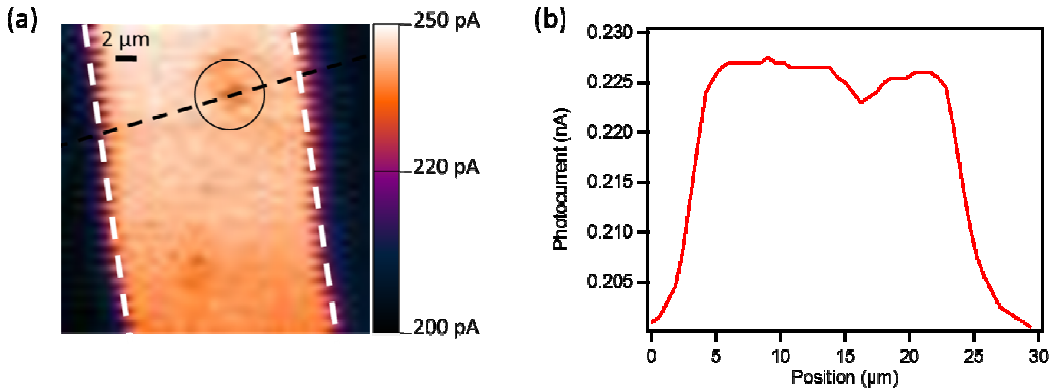

Figure 10: (a) Zero drain bias photocurrent response for OFET with 24% GNR/P3HT and ***L***=20 µm in the off-state (V_G=+30 V). The dashed white lines indicate the edges of the source and drain electrical contacts; the black circle indicates the observed aggregate of GNRs. (b) Variation of the photocurrent as a function of the position of the black dashed line in (a).

To gain more information about the local origin of the generated photoresponse and the role of the GNRs under illumination, we studied these devices using scanning photocurrent microscopy. This technique has been employed widely for the local photocurrent study of devices based on carbon nanotubes and graphene[84-88], and uses an optical microscope in combination with a multi-axis scanning stage for raster scanning the sample with respect to a laser beam focused on the device surface. We examined a device (***L***=20 µm) with 24% GNRs blended with P3HT at V_G=+30 V (in the off-state) and at zero source-drain bias under a ~1 µm spot size laser (λ=633 nm, power density < 50 kW cm^{-2}). The photocurrent image presented in Fig. 10 reveals uniform photocurrent response inside the channel indicating that the entire OFET channel is photoactive. However, a decrease in local photocurrent is observed in the areas where big aggregates of GNRs are present (see black circle in Fig. 10a and photocurrent profile in Fig. 10b). The difference could be explained by the fact that the photo-generated carriers in the aggregated region face higher impedance due to the potential barrier formed at the interface between the GNR aggregates (E_g GNR **1** = ~1.6eV) and P3HT (E_g P3HT = 1.9 - 2.0 eV) due the difference in their band gap (Fig. S5 in the ESI). Therefore this barrier results in a lower photocurrent collected on local illumination in this region of the channel. However, this small difference does

Nanoscale Accepted Manuscript

not strongly affect the overall performance of our phototransistors as demonstrated through measurements by illuminating the entire device area.

Conclusion

In summary, we have designed and synthesized a new $N = 18$ armchair graphene nanoribbons (GNR **1**) with a good dispersibility in organic solvents and an ionization energy matching that of P3HT. GNR **1** was blended with P3HT in a single step co-deposition process. While monocomponent GNR films suffer from the presence of macroscopic crystals alternated by domain boundaries, thereby lacks in terms of extended percolation pathways for charge transport, we have demonstrated that the addition of up to 24% of GNRs in a P3HT film enables improvement of percolation of charges in a P3HT transistor. In particular, it is possible to obtain a three-fold increase in the field-effect mobility in a P3HT device by adding 24% of GNRs to the thin film, without altering the other relevant electronic characteristics of the transistor such as the I_{on}/I_{off}. This behavior can be ascribed to the aggregates of GNRs acting as percolation patches for the charge carrier within the conduction channel by connecting the domains of the semiconductor film. The three-fold increase in μ is not outstanding because of the countereffects of the decrease in the crystalline nature in P3HT upon blending with GNR **1** and the formation of hundreds of nm large aggregates of GNR **1** as revealed by GIXD and AFM, respectively. Our P3HT – GNR blend approach, exhibiting an increased μ accompanied by an unaltered I_{on}/I_{off} ratio, represents a solution towards the enhancement of the performance of OFETs. The transistor's photoresponse in GNR – P3HT binary mixtures depends on the quantity of each component in the blend as well as on the channel length. This finding represents a step forward toward the potential use of these devices in (opto)electronics, where light can function as an additional control parameter.

Experimental section:

Materials

Nanoscale Accepted Manuscript

In this work, poly(3-hexylthiophene) (P3HT) (Figure 1b) (regioregularity >99%, Mw~50,000 g/mol, Sepiolid P-200 from BASF) was used as purchased. Other materials were purchased from Fluka, Aldrich, Acros, ABCR, Merck, and other commercial suppliers and used as received unless otherwise specified.

1,3-Di(biphenyl-3-yl)propan-2-on (**2**)

To a solution of 3-(bromomethyl)-biphenyl (17.6 g, 71.2 mmol), $Fe(CO)_5$ (7.3 g, 37 mmol), and benzyltriethylammonium chloride (0.54 g, 1.9 mmol) in dichloromethane (170 mL) was added a solution of potassium hydroxide (17.3 g, 307 mmol) in H_2O (9.0 ml), and the reaction mixture was refluxed over night. After cooling down to the room temperature the mixture was quenched with HCl, and the organic phase was concentrated in vacuo. The crude product was first purified by silica gel column chromatography (eluent: 6% ethyl acetate/hexane) and then dissolved in dichloromethane and reprecipitated from methanol to give the title compound as colorless crystals (5.31 g, 14.7 mmol, 41% yield): Mp: 104.3 °C; ^{1}H NMR (500 MHz, tetrahydrofuran-d_8, 303 K) δ = 7.56 (d, J = 7.3 Hz, 4H), 7.47 (d, J = 7.8 Hz, 2H), 7.44 (s, 2H), 7.37 (t, J = 7.7 Hz, 4H), 7.34 (t, J = 7.7 Hz, 2H), 7.28 (t, J = 7.4 Hz, 2H), 7.16 (d, J = 7.6 Hz, 2H), 3.83 (s, 4H); ^{13}C NMR (125 MHz, 1,2-tetrachloroethane-d_2, 303 K) δ = 205.65, 141.34, 140.40, 134.21, 129.06, 128.70, 128.41, 128.22, 127.39, 127.03, 125.81, 120.18, 49.14; MS (FD, 8 kV): m/z (%): 361.6 (100) [M^+] (calcd. for $C_{27}H_{22}O$: 362.2); Rf (30% ethyl acetate/hexane) = 0.75; Anal. found: C, 89.5; H, 6.3 (calcd. for $C_{27}H_{22}O$: C, 89.5; H, 6.1).

2,5-Di([1,1'-biphenyl]-3-yl)-3,4-bis(4-chlorophenyl)cyclopenta-2,4-dienone (**4**)

To a degassed solution of 4,4'-didochlorobenzil (**3**)[89] (940 mg, 3.37 mmol) and 1,3-di(biphenyl-3-yl)propan-2-on (**1**) (1.22 g, 3.37 mmol) in *tert*-butanol (20 mL) was added at 80 °C a methanol solution of tetrabutylammonium hydroxide (1.0 M, 1.7 ml, 1.7 mmol). After stirring at 80 °C for 20 min the reaction was quenched with water, and the reaction mixture was extracted three times with dichloromethane. The combined organic layers were washed with brine, dried over magnesium sulfate, and evaporated to give a purple crude product. Purification by silica gel column chromatography (eluent: 20% dichloromethane/hexane) gave the title compound as a purple solid (1.56 g, 2.58 mmol, 77% yield): ^{1}H NMR (700 MHz,

Nanoscale Accepted Manuscript

tetrahydrofuran-d_8) δ = 7.52 (s, 2H, CH), 7.50 (d, J = 7.8 Hz, 2H, CH), 7.42 (d, J = 7.2 Hz, 4H, CH), 7.36 (t, J = 7.7 Hz, 4H, CH), 7.32 (m, 6H, CH), 7.27 (t, J = 7.3 Hz, 2H, CH), 7.23 (d, J = 7.8 Hz, 2H, CH), 7.06 (d, J = 8.5 Hz, 4H, CH); ^{13}C NMR (175 MHz, tetrahydrofuran-d_8) δ = 199.86, 154.28, 141.91, 141.82, 135.61, 133.14, 132.14, 132.10, 129.98, 129.90, 129.70, 129.69, 129.52, 128.27, 127.78, 127.20, 126.73; MS (MALDI-TOF, positive): m/z: 604.6 [M^+] (calcd. for $C_{41}H_{26}Cl_2O$: 604.1); Rf (10% ethyl acetate/hexane) = 0.47.

1,2-Bis(4-chlorophenyl)-3,6-bis(biphenyl-3-yl)-4,5-bis(4-dodecylphenyl)benzene (**5**)

A degassed solution of 2,5-di([1,1'-biphenyl]-3-yl)-3,4-bis(4-chlorophenyl)cyclopenta-2,4-dienone (**4**) (1.84 g, 3.03 mmol) and bis(4-dodecylphenyl)acetylene[90] (1.72 g, 3.34 mmol) in diphenyl ether (12 mL) and propylene carbonate (5.0 mL) was stirred at 230 °C for 12 h twice under microwave irradiation with maximum power of 300 W and a maximum pressure of 7 bar. After cooling down to room temperature the reaction mixture was diluted with hexane and purified by silica gel column chromatography (eluent: 6% ethyl acetate/hexane). The product was further purified by using recycling preparative SEC (Waters Ultrastyragel 103 Å, 19 × 300 mm, eluent: chloroform, 3.0 mL/min) to give the title compound as colorless oil (1.85 g, 1.69 mmol, 56% yield): ^{1}H NMR (700 MHz, tetrahydrofuran-d_8) δ = 7.27 (dt, J = 7.7, 4.0 Hz, 4H, CH), 7.22–7.16 (m, 6H, CH), 7.10 (d, J = 10.0 Hz, 4H, CH), 6.94 (t, J = 7.7 Hz, 4H, CH), 6.91 (s, 2H), 6.88 (d, J = 8.4 Hz, 2H, CH), 6.87–6.81 (m, 2H, CH), 6.81–6.77 (m, 2H, CH), 6.77–6.70 (br m, 6H, CH), 6.66 (d, J = 7.5 Hz, 2H, CH), 2.41– 2.28 (m, 4H, α-CH_2), 1.44–1.34 (m, 4H, β-CH_2), 1.34–1.03 (m, 36H, -CH_2-), 0.89 (t, J = 6.9 Hz, 6H, -CH_3); ^{13}C NMR (175 MHz, tetrahydrofuran-d_8) δ = 142.44, 142.42, 142.27, 141.88, 141.74, 140.76, 140.74, 140.68, 140.59, 140.56, 140.14, 140.10, 139.09, 139.05, 134.18, 134.14, 134.06, 134.01, 132.56, 132.50, 132.47, 132.30, 132.26, 131.69, 131.41, 129.37, 128.20, 128.07, 127.90, 127.88, 127.84, 127.81, 127.80, 127.74, 125.14, 125.12, 36.36, 36.33, 33.06, 32.37, 32.34, 30.85, 30.81, 30.77, 30.75, 30.61, 30.60, 30.51, 30.00, 29.98, 25.94, 25.82, 23.74, 14.62; MS (MALDI-TOF, positive): m/z: 1091.0 [M^+] (calcd. for $C_{78}H_{84}Cl_2$: 1090.6); Rf (6% ethyl acetate/hexane) = 0.65; Anal. found: C, 85.6; H, 7.9 (calcd. for $C_{78}H_{84}Cl_2$: C, 85.8; H, 7.8).

Polyphenylene precursor **6**

Nanoscale Accepted Manuscript

The catalytic system consisting of $Ni(COD)_2$ (589 mg, 2.14 mmol), 1,5-cyclooctadiene (232 mg, 2.14 mmol), and 2,2'-bipyridine (334 mg, 2.14 mmol) in a mixture of DMF (2.0 mL) and toluene (2.0 mL) was prepared in a glove box under nitrogen atmosphere and wrapped in aluminum foil for the exclusion of light. The catalyst system was activated by stirring at 60 °C for 20 min, and then a degassed solution of 1,2-bis(4-chlorophenyl)-3,6-bis(biphenyl-3-yl)-4,5-bis(4-dodecylphenyl)benzene (**5**) (975 mg, 0.893 mmol) in dry toluene (2.0 mL) was added. The reaction mixture was stirred at 80 °C for 10 days. For endcapping of the resulting polymer an excess amount of chlorobenzene was added and heated for additional 20 minutes at 80 °C. After cooling down to the room temperature the reaction mixture was added dropwise to a mixture of hydrochloric acid and methanol (1:10), and stirred overnight. The precipitates were collected by centrifugation and then repeatedly reprecipitated from THF solution in methanol to give the title compound as a white solid (780 mg, 86% yield). A part of the polymer was fractionated by preparative SEC (Bio-Beads S-X1 support, Bio-Rad Laboratories), and then further by recycling preparative SEC to obtain a polymer fraction with $M_w = 1.0 \times 10^4$ gmol^{-1}, $M_n = 7.2 \times 10^3$ gmol^{-1}, and PDI = 1.4 as well as a fraction with $M_w = 1.2 \times 10^4$ gmol^{-1}, $M_n = 9.3 \times 10^3$ gmol^{-1}, and PDI = 1.3 based on SEC analysis (UV detector, polystyrene standard): FTIR (powder): 4052, 3084, 3054, 3029, 2924, 2852, 1598, 1573, 1513, 1498, 1479, 1465, 1451, 1407, 1356, 1259, 1184, 1141, 1118, 1092, 1074, 1053, 1021, 1006, 965, 944, 897, 841, 807, 717, 698 cm^{-1}.

GNR **1**

A solution of polyphenylene precursor **6** (76.6 mg) in unstabilized dichloromethane (80 mL) was degassed by argon bubbling for 15 min. To the solution was added a suspension of iron (III) chloride (1.10 g, 6.76 mmol) in nitromethane (3.5 mL). After stirring at room temperature for 3 days with a continuous argon flow through the reaction mixture, the reaction was quenched by the addition of methanol to form black precipitates, which were collected by centrifugation. The crude product was intensively washed with THF and methanol using Soxhlet extractor for 2 days to gave the title compound as black powder (72.9 mg, 98% yield): FTIR (powder): 2920, 2850, 1595, 1455, 1372, 864, 823, 802, 759, 740, 720 cm^{-1}; Raman (powder, 488 nm): 3200, 2922, 2725, 1578, 1325 cm^{-1}.

Nanoscale Accepted Manuscript

Solid-state NMR analysis

All solid-state ^{1}H NMR experiments were recorded on a Bruker AVANCE III 700 operating at a Larmor frequency of 700.21 MHz (16.45 T). The experiments employed a 1.3 mm H-X double-resonance magic-angle spinning (MAS) probe from Bruker, using a spinning frequency of 59524 Hz and a π/2-pulse length of 1.5 μs, corresponding to an rf-field strength of 167 kHz. The 2D ^{1}H-^{1}H double quantum-single quantum (DQ-SQ) correlation experiments were recorded using the compensated Back-to-Back (BaBa) dipolar recoupling sequence for both excitation and reconversion of DQ coherences followed by a z-filter, set to one rotor period, prior to a final π/2 pulse for creating transverse observable magnetization.[62, 63] A phase cycling scheme of 16 steps, a recycle delay of 2 s, and 16 scans per rotor-synchronized t_1 increment were used. Prior to all experiments the magic angle was checked with KBr.[91] ^{1}H chemical shifts are reported relative to TMS using solid adamantane as an external reference.[92] The 2D ^{1}H-^{1}H DQ-SQ spectra shown in Figure 4 were processed identically and plotted on the same intensity scale with 22 contour lines from 2.0% to 90% of the maximum intensity.

Device fabrication

Bottom-gate bottom contact transistors exposing 230 nm thermally grown oxide on n++-doped silicon (Fraunhofer Institute, capacitance 1.5×10^{-8} F/cm^2) were used. Each substrate exposes prepatterned interdigitated Au source-drain electrodes with different channel length (***L*** = 2.5, 5, 10, 20 μm) and constant channel width (***W*** = 10 mm). These substrates were cleaned in an ultrasonic bath of acetone and isopropanol prior to device fabrication. For the devices with higher channel length (***L*** = 60, 80, 100, 120 μm) and same width (***W*** = 10 mm), interdigitated Au source-drain electrodes (40 nm) were evaporated (chamber pressure = 10^{-6} mbar, evaporation rate = 0.03 nm/s) on bare SiO_x substrates (having the same specifications as above mentioned) using a shadow mask. GNRs were dispersed in ODCB and sonicated for at least 90 min then immediately transferred to the glove box (N_2 atmosphere) where they were mixed with a constant amount of P3HT (1.5 mg/mL in ODCB) at different percentages (2, 5, 11 and 24 wt % with respect to P3HT). Thin films were prepared inside the glovebox (N_2 atmosphere) by spin-coating the blend at 1200 rpm for 60 sec onto untreated substrates. This was followed by an

Nanoscale Accepted Manuscript

annealing step at 200 °C for 15 min. For comparison, we prepared pristine P3HT devices that were processed in the same fashion as for the blended ones.

Electrical characterization of the devices

Electrical characterization of the devices was performed at room temperature in a N_2 atmosphere inside a glovebox, using a Cascade Microtech M150 probe station and a Keithley 2636A sourcemeter as semiconductor parameter analyzer controlled by associated software.

To study the photoresponse, at least 6 devices for each channel length and each blend percentage were characterized under illumination from the top using a Polychrome V (Till Photonics) tunable light source providing a monochromatic beam with 605 nm and 560 nm wavelengths and irradiance levels of 8.17 and 9.44 mW/cm^2 respectively. The light intensity was measured using an analog optical power meter, PM100A (ThorLabs). These wavelengths were chosen in view of the absorbance spectra and correspond to two absorption peaks of the P3HT films as shown in Fig. S12 electronic supplementary information (ESI). The measurement sequence used is as follows: two consecutive measurements for transfer and output characteristics in dark. The light is then switched on, and transfer and output characteristics under illumination are measured. For some devices only, this was followed by measurements in dark after 5 min of switching off the light to see if there is a photo-induced memory effect.

To study the relaxation of the photo-induced charges, 5 to 6 devices of $\boldsymbol{L}$=20 µm for each blend percentage were characterized under illumination at λ=560 nm (9.44 mW/cm^2). Two measurement sequences were used: in the first case, continuous gate bias V_G=0 V and drain bias V_D=-10 V were applied in dark for 30 sec then the light is switched on for 30 sec then switched off for 30 sec. whereas in the second case the same was followed except that the gate was floating (no gate bias applied).

Photocurrent mapping

Nanoscale Accepted Manuscript

Photocurrent mapping was done using a laser light (λ=633 nm, power density < 50 $kW \cdot cm^{-2}$) generated from a He–Ne laser which was coupled to the sample by using a DM LM microscope (Leica) and a ×100 ultra-long working distance objective, resulting in a ~1 μm spot size. A Physik Instrument piezoelectric stage was used to translate the device with respect to the laser spot in the x/y directions with 500 nm steps, resulting in confocal, position-dependent recording of the generated photocurrent. Measurements were done at room temperature with a low pressure N_2 flow over the sample. Photocurrent signals were recorded by modulating the laser beam (1 kHz) using a mechanical chopper and the short circuit photocurrent was detected by lock-in amplifier. A 2400 Sourcemeter (Keithley) was employed to control the gate voltage. For this experiment, in order to overcome the air sensitivity issue of P3HT, an encapsulating film of poly(methyl methacrylate) (PMMA) (70 mg/mL in Methyl Ethyl Ketone) was spin coated onto the devices at 1000 rpm for 30 sec, 200 μL (see supporting information for more details).

Instrumentation

Atomic Force Microscopy (AFM) images were recorded using Nanoscope (Veeco Multimode V). Measurements of the thickness of the active layer were performed using Alpha step IQ profiler. Scanning electron microscopy (SEM) images for pure GNRs were taken using Strata 400 Dual Beam. Samples were prepared by drop casting (0.25 mg/mL in ODCB) followed by annealing at 200°C for 15 min then sputtered with Au (30 sec, I=60 mA). Ambient photoelectron spectroscopy measurements were performed on drop casted films (annealed at 200 °C for 15 min inside the glovebox) using a new generation of photoelectron spectroscopies operating at atmospheric conditions (RIKEN AC-2). The same instrument was used for determining the work function of Au thin film prepared by vacuum evaporation (at $P=1.7 \times 10^{-6}$ mbar) onto mica substrates (45ºC). X-ray diffraction (GIXD) measurements were performed using the grazing-incidence geometry. The experimental setup included a rotating copper anode X-ray source (Rigaku Micromax, operated at 42 kV and 20 mA), Osmic confocal MaxFlux optics and a three x/y-adjustable pin-hole collimation system (JJ X-ray). Samples deposited on top of silicone substrates were irradiated with a wavelength of λ=1.5418 Å at the incident angle (α_i) of 0.11°. The GIXD patterns were recorded for 5 hrs on a MAR345 image plate detector. Camera length

Nanoscale Accepted Manuscript

(315 mm) and the range of detectable d-spacings (~35 Å $<d_{hkl}<$3 Å) were calibrated using silver behenate standard. The data was processed using Datasqueeze 2.2.9 program.

Acknowledgments

This work was financially supported by the EC - Marie-Curie ITNs GENIUS (PITN-GA-2010-264694) and SUPERIOR (PITN-GA-2009-238177), the Graphene Flagship (GA-604391), and the International Center for Frontier Research in Chemistry (icFRC). AK acknowledges support from the Marie Curie project (PIEF-GA-2009-253521) and the statutory activity subsidy for the Faculty of Chemistry of Wroclaw University of Technology.

† Electronic Supplementary Information (ESI) available: [details of any supplementary information available should be included here]. See DOI: 10.1039/b000000x/

Nanoscale Accepted Manuscript

References

1. H. Yan, Z. Chen, Y. Zheng, C. Newman, J. R. Quinn, F. Dotz, M. Kastler and A. Facchetti, *Nature*, 2009, **457**, 679.
2. B. C. Schroeder, C. B. Nielsen, Y. J. Kim, J. Smith, Z. Huang, J. Durrant, S. E. Watkins, K. Song, T. D. Anthopoulos and I. McCulloch, *Chem. Mater.*, 2011, **23**, 4025.
3. I. McCulloch, R. S. Ashraf, L. Biniek, H. Bronstein, C. Combe, J. E. Donaghey, D. I. James, C. B. Nielsen, B. C. Schroeder and W. Zhang, *Acc. Chem. Res.*, 2012, **45**, 714.
4. J. E. Anthony, *Chem. Rev.*, 2006, **106**, 5028.
5. J. E. Anthony, A. Facchetti, M. Heeney, S. R. Marder and X. W. Zhan, *Adv. Mater.*, 2010, **22**, 3876.
6. A. C. Arias, J. D. MacKenzie, I. McCulloch, J. Rivnay and A. Salleo, *Chem. Rev.*, 2010, **110**, 3.
7. A. Facchetti, *Mater Today*, 2007, **10**, 28.
8. I. McCulloch, M. Heeney, C. Bailey, K. Genevicius, M. I, M. Shkunov, D. Sparrowe, S. Tierney, R. Wagner, W. M. Zhang, M. L. Chabinyc, R. J. Kline, M. D. Mcgehee and M. F. Toney, *Nat. Mater.*, 2006, **5**, 328.
9. X. W. Zhan, A. Facchetti, S. Barlow, T. J. Marks, M. A. Ratner, M. R. Wasielewski and S. R. Marder, *Adv. Mater.*, 2011, **23**, 268.
10. M. Zhang, H. N. Tsao, W. Pisula, C. D. Yang, A. K. Mishra and K. Müllen, *J. Am. Chem. Soc.*, 2007, **129**, 3472.
11. J. Smith, R. Hamilton, Y. Qi, A. Kahn, D. D. C. Bradley, M. Heeney, I. McCulloch and T. D. Anthopoulos, *Adv. Funct. Mater.*, 2010, **20**, 2330.
12. E. Orgiu, A. M. Masillamani, J.-O. Vogel, E. Treossi, A. Kiersnowski, M. Kastler, W. Pisula, F. Dotz, V. Palermo and P. Samorì, *Chem. Commun.*, 2012, **48**, 1562.
13. R. Dabirian, V. Palermo, A. Liscio, E. Schwartz, M. B. J. Otten, C. E. Finlayson, E. Treossi, R. H. Friend, G. Calestani, K. Müllen, R. J. M. Nolte, A. E. Rowan and P. Samorì, *J. Am. Chem. Soc.*, 2009, **131**, 7055.
14. J. Smith, W. Zhang, R. Sougrat, K. Zhao, R. Li, D. Cha, A. Amassian, M. Heeney, I. McCulloch and T. D. Anthopoulos, *Adv. Mater.*, 2012, **24**, 2441.
15. R. Hamilton, J. Smith, S. Ogier, M. Heeney, J. E. Anthony, I. McCulloch, J. Veres, D. D. C. Bradley and T. D. Anthopoulos, *Adv. Mater.*, 2009, **21**, 1166.
16. E. Lim, B. J. Jung, M. Chikamatsu, R. Azumi, K. Yase, L. M. Do and H. K. Shim, *Org. Electron.*, 2008, **9**, 952.
17. D. M. Russell, C. J. Newsome, S. P. Li, T. Kugler, M. Ishida and T. Shimoda, *Appl. Phys. Lett.*, 2005, **87**.
18. J. Smith, R. Hamilton, M. Heeney, D. M. de Leeuw, E. Cantatore, J. E. Anthony, I. McCulloch, D. D. C. Bradley and T. D. Anthopoulos, *Appl. Phys. Lett.*, 2008, **93**.
19. J. Smith, R. Hamilton, Y. B. Qi, A. Kahn, D. D. C. Bradley, M. Heeney, I. McCulloch and T. D. Anthopoulos, *Adv. Funct. Mater.*, 2010, **20**, 2330.
20. E. Orgiu, N. Crivillers, M. Herder, L. Grubert, M. Pätzel, J. Frisch, E. Pavlica, D. T. Duong, G. Bratina, A. Salleo, N. Koch, S. Hecht and P. Samorì, *Nat Chem*, 2012, **4**, 675.
21. K.-J. Baeg, D. Khim, D.-Y. Kim, J. B. Koo, I.-K. You, W. S. Choi and Y.-Y. Noh, *Thin Solid Films*, 2010, **518**, 4024.

Nanoscale Accepted Manuscript

22. Z. Bao, A. Dodabalapur and A. J. Lovinger, *Appl. Phys. Lett.*, 1996, **69**, 4108.
23. Y. Fu, C. Lin and F.-Y. Tsai, *Org. Electron.*, 2009, **10**, 883.
24. M. Surin, P. Leclere, R. Lazzaroni, J. D. Yuen, G. Wang, D. Moses, A. J. Heeger, S. Cho and K. Lee, *J. Appl. Phys.*, 2006, **100**, 033712.
25. H. Sirringhaus, P. J. Brown, R. H. Friend, M. M. Nielsen, K. Bechgaard, B. M. W. Langeveld-Voss, A. J. H. Spiering, R. A. J. Janssen, E. W. Meijer, P. Herwig and D. M. de Leeuw, *Nature*, 1999, **401**, 685.
26. J. Huang, D. R. Hines, B. J. Jung, M. S. Bronsgeest, A. Tunnell, V. Ballarotto, H. E. Katz, M. S. Fuhrer, E. D. Williams and J. Cumings, *Org. Electron.*, 2011, **12**, 1471.
27. A. Liscio, G. P. Veronese, E. Treossi, F. Suriano, F. Rossella, V. Bellani, R. Rizzoli, P. Samorì and V. Palermo, *J. Mater. Chem.*, 2011, **21**, 2924.
28. X. Z. Bo, C. Y. Lee, M. S. Strano, M. Goldfinger, C. Nuckolls and G. B. Blanchet, *Appl. Phys. Lett.*, 2005, **86**, 182102.
29. Y. D. Park, J. A. Lim, Y. Jang, M. Hwang, H. S. Lee, D. H. Lee, H.-J. Lee, J.-B. Baek and K. Cho, *Org. Electron.*, 2008, **9**, 317.
30. K. S. Novoselov, A. K. Geim, S. V. Morozov, D. Jiang, Y. Zhang, S. V. Dubonos, I. V. Grigorieva and A. A. Firsov, *Science*, 2004, **306**, 666.
31. C. Mattevi, F. Colléaux, H. Kim, Y. H. Lin, K. T. Park, M. Chhowalla and T. D. Anthopoulos, *Nanotechnology*, 2012, **23**.
32. C.-A. Palma and P. Samorì, *Nat Chem*, 2011, **3**, 431.
33. L. Chen, Y. Hernandez, X. Feng and K. Müllen, *Angew. Chem. Int. Ed.*, 2012, **51**, 7640.
34. M. Y. Han, B. Özyilmaz, Y. Zhang and P. Kim, *Phys. Rev. Lett.*, 2007, **98**, 206805.
35. B. Ozyilmaz, P. Jarillo-Herrero, D. Efetov and P. Kim, *Appl. Phys. Lett.*, 2007, **91**, 192107.
36. D. Yoon, H. Moon, H. Cheong, J. S. Choi, J. A. Choi and B. H. Park, *Journal of the Korean Physical Society*, 2009, **55**, 1299.
37. L. Jiao, L. Zhang, X. Wang, G. Diankov and H. Dai, *Nature*, 2009, **458**, 877.
38. D. V. Kosynkin, A. L. Higginbotham, A. Sinitskii, J. R. Lomeda, A. Dimiev, B. K. Price and J. M. Tour, *Nature*, 2009, **458**, 872.
39. ShimizuT, HaruyamaJ, D. C. Marcano, D. V. Kosinkin, J. M. Tour, HiroseK and SuenagaK, *Nat. Nanotech.*, 2011, **6**, 45.
40. X. Li, X. Wang, L. Zhang, S. Lee and H. Dai, *Science*, 2008, **319**, 1229.
41. L. Dössel, L. Gherghel, X. Feng and K. Müllen, *Angew. Chem. Int. Ed.*, 2011, **50**, 2540.
42. M. G. Schwab, A. Narita, Y. Hernandez, T. Balandina, K. S. Mali, S. De Feyter, X. Feng and K. Müllen, *J. Am. Chem. Soc.*, 2012, **134**, 18169.
43. J. Wu, L. Gherghel, M. D. Watson, J. Li, Z. Wang, C. D. Simpson, U. Kolb and K. Müllen, *Macromolecules*, 2003, **36**, 7082.
44. X. Yang, X. Dou, A. Rouhanipour, L. Zhi, H. J. Räder and K. Müllen, *J. Am. Chem. Soc.*, 2008, **130**, 4216.
45. J. Cai, P. Ruffieux, R. Jaafar, M. Bieri, T. Braun, S. Blankenburg, M. Muoth, A. P. Seitsonen, M. Saleh, X. Feng, K. Müllen and R. Fasel, *Nature*, 2010, **466**, 470.
46. P. Rempala, J. Kroulík and B. T. King, *J. Am. Chem. Soc.*, 2004, **126**, 15002.
47. R. Scholl and C. Seer, *Justus Liebigs Annalen der Chemie*, 1912, **394**, 111.
48. S. Osella, A. Narita, M. G. Schwab, Y. Hernandez, X. Feng, K. Müllen and D. Beljonne, *ACS Nano*, 2012, **6**, 5539.
49. T. Yamamoto, *Prog. Polym. Sci.*, 1992, **17**, 1153.

Nanoscale Accepted Manuscript

50. T. Yamamoto, *Bull. Chem. Soc. Jpn.*, 1999, **72**, 621.
51. J. Sakamoto, M. Rehahn, G. Wegner and A. D. Schlüter, *Macromol. Rapid Commun.*, 2009, **30**, 653.
52. A. Narita, X. Feng, Y. Hernandez, S. A. Jensen, M. Bonn, H. Yang, I. A. Verzhbitskiy, C. Casiraghi, M. R. Hansen, A. H. R. Koch, G. Fytas, O. Ivasenko, B. Li, K. S. Mali, T. Balandina, S. Mahesh, S. De Feyter and K. Müllen, *Nat Chem*, 2014, **6**, 126.
53. K. Martin, J. Spickermann, H. J. Räder and K. Müllen, *Rapid Commun. Mass Spectrom.*, 1996, **10**, 1471.
54. A. Centrone, L. Brambilla, T. Renouard, L. Gherghel, C. Mathis, K. Müllen and G. Zerbi, *Carbon*, 2005, **43**, 1593.
55. Z. B. Shifrina, M. S. Averina, A. L. Rusanov, M. Wagner and K. Müllen, *Macromolecules*, 2000, **33**, 3525.
56. J. Shu, D. Dudenko, M. Esmaeili, J. H. Park, S. R. Puniredd, J. Y. Chang, D. W. Breiby, W. Pisula and M. R. Hansen, *J. Am. Chem. Soc.*, 2013, **135**, 11075.
57. S. P. Brown, *Solid State Nucl. Magn. Reson.*, 2012, **41**, 1.
58. N. Tasios, C. Grigoriadis, M. R. Hansen, H. Wonneberger, C. Li, H. W. Spiess, K. Müllen and G. Floudas, *J. Am. Chem. Soc.*, 2010, **132**, 7478.
59. A. Bohle, G. Brunklaus, M. R. Hansen, T. W. Schleuss, A. F. M. Kilbinger, J. Seltmann and H. W. Spiess, *Macromolecules*, 2010, **43**, 4978.
60. M. R. Hansen, X. Feng, V. Macho, K. Müllen, H. W. Spiess and G. Floudas, *Phys. Rev. Lett.*, 2011, **107**, 257801.
61. M. M. Elmahdy, X. Dou, M. Mondeshki, G. Floudas, H.-J. Butt, H. W. Spiess and K. Müllen, *J. Am. Chem. Soc.*, 2008, **130**, 5311.
62. K. Saalwächter, F. Lange, K. Matyjaszewski, C.-F. Huang and R. Graf, *J. Magn. Reson.*, 2011, **212**, 204.
63. M. Feike, D. E. Demco, R. Graf, J. Gottwald, S. Hafner and H. W. Spiess, *Journal of Magnetic Resonance, Series A*, 1996, **122**, 214.
64. D. Sebastiani and K. N. Kudin, *ACS Nano*, 2008, **2**, 661.
65. Z. Chen, C. S. Wannere, C. Corminboeuf, R. Puchta and P. v. R. Schleyer, *Chem. Rev.*, 2005, **105**, 3842.
66. F. Torrisi, T. Hasan, W. Wu, Z. Sun, A. Lombardo, T. S. Kulmala, G.-W. Hsieh, S. Jung, F. Bonaccorso, P. J. Paul, D. Chu and A. C. Ferrari, *ACS Nano*, 2012, **6**, 2992.
67. D. M. Russell, C. J. Newsome, S. P. Li, T. Kugler, M. Ishida and T. Shimoda, *Appl. Phys. Lett.*, 2005, **87**, 222109.
68. D. Dudenko, A. Kiersnowski, J. Shu, W. Pisula, D. Sebastiani, H. W. Spiess and M. R. Hansen, *Angew. Chem. Int. Ed.*, 2012, **51**, 11068.
69. N. Kayunkid, S. Uttiya and M. Brinkmann, *Macromolecules*, 2010, **43**, 4961.
70. K. Rahimi, I. Botiz, N. Stingelin, N. Kayunkid, M. Sommer, F. P. V. Koch, H. Nguyen, O. Coulembier, P. Dubois, M. Brinkmann and G. Reiter, *Angew. Chem. Int. Ed.*, 2012, **51**, 11131.
71. X. Wang, Y. Ouyang, X. Li, H. Wang, J. Guo and H. Dai, *Phys. Rev. Lett.*, 2008, **100**, 206803.
72. K. T. Kim, J. W. Jung and W. H. Jo, *Carbon*, 2013, **63**, 202.
73. T. Pal, M. Arif and S. Khondaker, *Nanotechnology*, 2010, **21**, 325201.
74. M. EL Gemayel, M. Treier, C. Musumeci, C. Li, K. Müllen and P. Samorì, *J. Am. Chem. Soc.*, 2012, **134**, 2429.

Nanoscale Accepted Manuscript

75. M. J. Deen and M. H. Kazemeini, *Proceedings of the IEEE*, 2005, **93**, 1312.
76. M. C. Hamilton and J. Kanicki, *IEEE J. Sel. Top. Quantum Electron.*, 2004, **10**, 840.
77. M. C. Hamilton, S. Martin and J. Kanicki, *IEEE Trans. Electron Dev.*, 2004, **51**, 877.
78. N. Marjanović, T. B. Singh, G. Dennler, S. Günes, H. Neugebauer, N. S. Sariciftci, R. Schwödiauer and S. Bauer, *Org. Electron.*, 2006, **7**, 188.
79. T. P. I. Saragi, M. Fetten and J. Salbeck, *Appl. Phys. Lett.*, 2007, **90**, 253506.
80. K. Wasapinyokul, W. I. Milne and D. P. Chu, *J. Appl. Phys.*, 2011, **109**, 084510.
81. *R=150 A•W^{-1} (at V_G=-80 V) and P=103 for (**L**=3 μm) prepared by drop casting and studied under white light (51 mW/cm^2).*
82. G. Dicker, M. P. de Haas, D. M. de Leeuw and L. D. A. Siebbeles, *Chem. Phys. Lett.*, 2005, **402**, 370.
83. S. Dutta and K. S. Narayan, *Phys. Rev. B*, 2003, **68**, 125208.
84. M. Burghard and A. Mews, *ACS Nano*, 2012, **6**, 5752.
85. M. Engel, M. Steiner, R. S. Sundaram, R. Krupke, A. A. Green, M. C. Hersam and P. Avouris, *ACS Nano*, 2012, **6**, 7303.
86. R. S. Sundaram, M. Steiner, H. Y. Chiu, M. Engel, A. A. Bol, R. Krupke, M. Burghard, K. Kern and P. Avouris, *Nano Lett.*, 2011, **11**, 3833.
87. E. J. H. Lee, K. Balasubramanian, R. T. Weitz, M. Burghard and K. Kern, *Nat. Nanotech.*, 2008, **3**, 486.
88. E. J. H. Lee, K. Balasubramanian, J. Dorfmuller, R. Vogelgesang, N. Fu, A. Mews, M. Burghard and K. Kern, *Small*, 2007, **3**, 2038.
89. D. C. Neckers and G. Hauck, *J. Org. Chem.*, 1983, **48**, 4691.
90. T. Izawa, E. Miyazaki and K. Takimiya, *Chem. Mater.*, 2009, **21**, 903.
91. J. S. Frye and G. E. Maciel, *J. Magn. Reson.*, 1982, **48**, 125.
92. S. Hayashi and K. Hayamizu, *Bull. Chem. Soc. Jpn.*, 1991, **64**, 685.

Nanoscale Accepted Manuscript